Available online at www.sciencedirect.com
ScienceDirect
Trans. Nonferrous Met. Soc. China 33(2023) 539−552
Transactions of Nonferrous Metals Society of China
www.tnmsc.cn

Redox-mediated in-situ fabrication of nanoparticle-packed porous Ag films with excellent surface-enhanced Raman scattering performance

Hao LEI[1,2], Yan LI[1], Meng-wei GUO[1], Qi-bo ZHANG[1,3]

1. Key Laboratory of Ionic Liquids Metallurgy, Faculty of Metallurgical and Energy Engineering, Kunming University of Science and Technology, Kunming 650093, China;
2. Shenzhen Key Laboratory of Flexible Printed Electronics Technology, Harbin Institute of Technology (Shenzhen), Shenzhen 518055, China;
3. State Key Laboratory of Complex Nonferrous Metal Resources Cleaning Utilization in Yunnan Province, Kunming University of Science and Technology, Kunming 650093, China

Received 26 October 2021; accepted 29 March 2022

Abstract: Smooth Ag substrate achieved in-situ conversion to form nanoporous architecture that is assembled by highly dispersed nanoparticles (NPs) with a mean size of 21.88 nm by applying a redox potential signal in an alkaline solution with an appropriate pH range. The detailed phase constitution and microstructure evolution process of the Ag substrate induced by the electrochemical redox tuning approach were systemically investigated. Under the action of controllable redox potentials, the smooth Ag substrate is firstly electrochemically oxidized to form Ag_2O with an expansion on the unit volume, followed by electrochemical reduction back to metallic Ag, causing the cell volume to shrink. The expansion and contraction of the unit volume during the highly reversible electrochemical process lead to in-situ formation of the highly porous Ag architectures. The fabricated Ag NPs-packed electrode exhibits as an excellent surface-enhanced Raman scattering (SERS) performance, and the measured Raman spectrum of Rhodamine 6G (R6G) reaches a detection limit of 5.44×10^{-10} mol/L.

Key words: electrochemical redox; silver nanoparticles; porous film; surface-enhanced Raman scattering performance

1 Introduction

Precious metal-based nanomaterials have attracted more and more attention in recent years. They not only possess metal properties such as excellent thermal stability and durability, high electrical conductivity, and catalytic activity, but also display excellent structural properties, including high surface area, ultra-low density, and high specific strength. In particular, the size effect of nanostructured metals obviously enhances their catalytic activity [1−3] and plasmon resonance [4,5], highlighting the advantage of nanometals relative to the form of metal blocks. Among them, nanostructured Ag is a kind of typical relatively inexpensive precious metal materials with excellent properties such as strong plasmon resonance effect, high conductivity and reactivity. It has broad application prospects in optical sensors [6−8], surface-enhanced Raman scattering (SERS) [4,9] and carbon dioxide electrical reduction [10,11].

In the past few decades, various methods have been developed to rationally design and customize nanometals with adjustable structures, and most of them are based on templating [12−14] and de-alloying methods [15,16]. The templating method is highly dependent on templates and has

Corresponding author: Yan LI, Tel: +86-871-65162008, Fax: +86-871-65161278, E-mail: kmliyan@163.com; Qi-bo ZHANG, E-mail: qibozhang@kust.edu.cn
DOI: 10.1016/S1003-6326(22)66126-0

the following problems: (1) due to the imperfection of the template and the complicated fabrication process, the obtained nanostructure is incomplete occasionally; (2) the cost is relatively high; (3) the mass production is difficult, which seriously restricts its large-scale application. In contrast, the de-alloying methodology, on the other hand, especially the electrochemical de-alloying approach, has been considered to be an efficient way to produce three-dimensional nanoporous metals with an open and double-continuous ligament pore structure due to the low working temperature required, short synthesis time, and strong controllability [15]. Nevertheless, limited by the electrochemical window of the electrolyte and the relatively high requirements for the alloy precursors, currently only some metals (Au [17], Cu [18,19], Pt [20] and Mn [21]) with a well-defined nanometer scale can be prepared by the electrochemical de-alloying approach. Some scientists, however, are working on more promising alternative synthesis methods [13,22]. Although enormous advances have been made to fabricate nanostructured metals with enhanced electrochemical performance, to prepare nanomaterials quickly, concisely, and reproducibly is an ongoing challenge.

In this work, we report a novel procedure to in-situ fabricate highly porous Ag films with smooth Ag substrate through a controllable electrochemical redox tuning approach in alkaline solution at room temperature. An electrochemically driven phase conversion process along with the change in the unit cell volume of Ag species is observed. Driven by controllable redox potentials, the smooth Ag substrate is firstly electrochemically oxidized to form Ag_2O with an expansion on the unit volume, followed by reversely electrochemical reduction back to metallic Ag, causing the cell volume to shrink. The expansion and contraction of the unit volume during the electrochemical tuning process result in the formation of the highly porous Ag architectures. The results reveal that the porous size and ligament structure can be easily mediated by carefully controlling the electrochemical redox tuning process. The optimized porous Ag film fabricated exhibits significantly enhanced SERS sensitivity with R6G as the Raman active probe. With the much enhanced Raman sensitivity, the prepared Ag-based SERS substrate could be applied to reliable analysis of the R6G concentration. The proposed manufacture may open up a new scalable technique for the design and fabrication of self-assembly Ag-based electrodes for practical SERS applications.

2 Experimental

2.1 Chemicals and reagents

Potassium hydroxide (KOH, 98%), Rhodamine 6G (R6G, 99 %), and Milli-Q deionized water (18.2 MΩ·cm) were purchased from Aladdin Ltd., China All the reagents were of analytical purity and were used without further purification. Deionized water was used through for all the solutions during the preparation. Ag plates (purity >99.99%) were purchased from Sinopharm Chemical Reagent Co., Ltd., China

2.2 Synthesis of Ag NPs-packed film

The Ag NPs-packed film was synthesized using an electrochemical workstation (Shanghai Chenhua 760E) with a standard three-electrode system at room temperature. The working, reference, and counter electrodes were Ag plate (electrode area: 1 cm × 3 cm; area immersed in the solution: 1 cm × 1 cm), saturated calomel electrode, and graphite rod (exposed area: 1.57 cm^2), respectively. For a typical synthesis, a smooth Ag plate was immersed in 0.1 mol/L KOH solution by applying a controllable redox potential signal, named as an in-situ electrochemical redox tuning process. Both electrochemical oxidation (ECO) and electrochemical reduction (ECR) were achieved through multiple linear voltammetry scans at a scan rate of 20 mV/s (ECO: 1.2−1.8 V (vs RHE); ECR: 1.4−0.2 V (vs RHE)). After the redox process, the prepared sample was taken out, repeatedly washed with absolute ethanol and deionized water, and then dried in air.

2.3 SERS signal detection

2.3.1 Measurement method

The SERS-enhanced performance of the prepared Ag NPs-packed film was examined by using R6G dye molecules as the probe molecules. Firstly, 0.48 g R6G was dissolved in 100 mL deionized water and further diluted to different concentrations. Subsequently, 150 μL of the dilution

was dispersed on a 1.0 cm^2 sample and dried. The R6G SERS spectrum was obtained by detecting the sample with a Renishaw Invia Reflex micro-Raman spectrophotometer (Renishaw plc, Wotton-under-Edge, UK) equipped with a cooled CCD (charge-coupled device) camera, and by selecting a 632.8 nm helium−neon laser source (Melles-Griot, USA). The laser power was around 35 mW. All the spectra were baseline corrected.

2.3.2 Enhancement factors

The SERS enhancement properties of given nanostructures can be represented by enhancement factors (EFs, E_f), and the calculation formula is as follows [23]:

$$E_f = \frac{I_{SERS}/N_{SERS}}{I_0/N_0} \quad (1)$$

where I_{SERS} is the Raman signal intensity obtained by a given nanostructure under consideration, and N_{SERS} is the number of R6G molecules irradiated for the SERS measurement (to obtain the E_f of the prepared Ag NPs-packed film, a smooth Ag substrate was used for comparison), I_0 is the Raman intensity obtained on a smooth Ag substrate, and N_0 is the number of R6G molecules irradiated by laser light on a smooth Ag substrate. Since the volume of the R6G solution dropped into the two substrates is the same (1 mL), the E_f value can be obtained according to the following equation [24]:

$$E_f = \frac{I_{SERS}/c_{SERS}}{I_0/c_0} \quad (2)$$

where c_{SERS} is the corresponding R6G molecules concentration, and c_0 is the number of R6G molecules dispersed on a smooth Ag substrate.

2.4 Characterization

X-ray diffraction (XRD) pattern was recorded on a Rigaku X-ray diffractometer (MinifexII Desktop) with high-intensity Cu K_α radiation. Field emission scanning electron microscopy measurement (FESEM; Nova 400 Nano-SEM) was carried out at an accelerated voltage of 15 kV. Transmission electron microscopy (TEM) measurement was performed at 200 kV using a Tecnai G2 TF30 transmission microscope. The topological change of the sample during the redox process was detected by a tapping mode atomic force microscope (AFM, SPI3800N).

3 Results and discussion

3.1 Formation mechanism of Ag NPs-packed film

Significant morphological changes upon the treatment by the proposed electrochemical redox tuning approach can be observed from the typical SEM images, as shown in Fig. 1. The smooth surface of the pristine Ag substrate was changed to a rough framework consisting of irregular nanoblocks after 15 times of in-situ ECO (denoted as Ag NPs_ECO15), and further developed to well-defined NPs-packed porous architectures followed by 4 times of ECR (denoted as Ag NPs_ECO15-ECR4). Accordingly, the measured average particle size of Ag NPs was changed from 41.45 nm for in-situ ECO treatment to 21.88 nm, followed by ECR process (Insets in Figs. 1(b) and (c)).

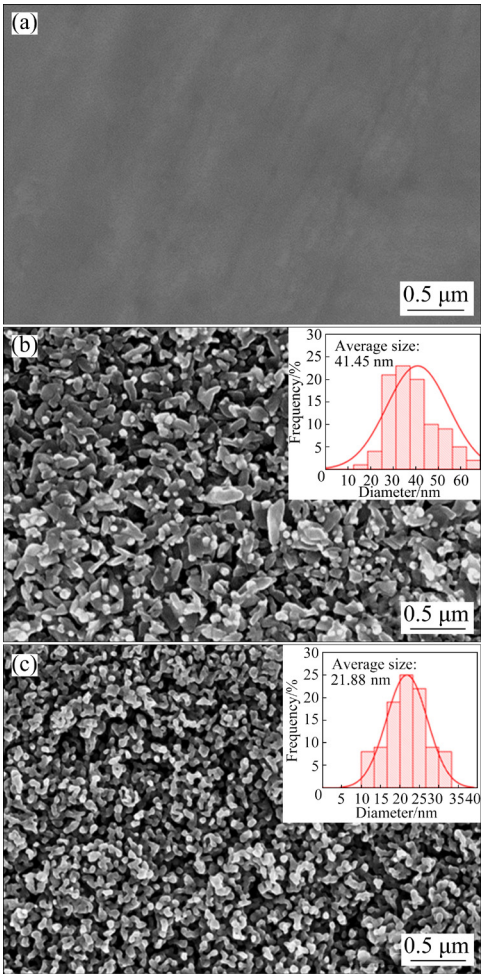

Fig. 1 SEM images of pristine smooth Ag (a), Ag NPs_ECO15 (b), and Ag NPs_ECO15-ECR4 (c) (The insets are particle size distributions of Ag NPs_ECO15 and Ag NPs_ECO15-ECR4, respectively)

To investigate the morphology evolution of the Ag nanostructures from a perspective of solvent thermodynamics, the potential−pH equilibrium diagram of the Ag−H_2O system at 298 K was developed from the standard free energies of the constituents (Fig. 2(a)). It is clear that under alkaline conditions (10<pH<14), Ag undergoes in-situ oxidation at a higher oxidation potential (0.463 V (vs RHE)) to form Ag_2O. Further increasing the oxidation potential will further oxidize Ag to produce AgO or even silver peroxide (Ag_2O_3). Obviously, if the pH of the system is not well controlled, Ag will dissolve into the solution as ions, either in the form of Ag^+ (pH<10) or AgO^- (pH>14). Obviously, an appropriate pH value of solution is a necessary condition for the in-situ electrochemical synthesis strategy. In this study, a 0.1 mol/L KOH aqueous solution with a pH value

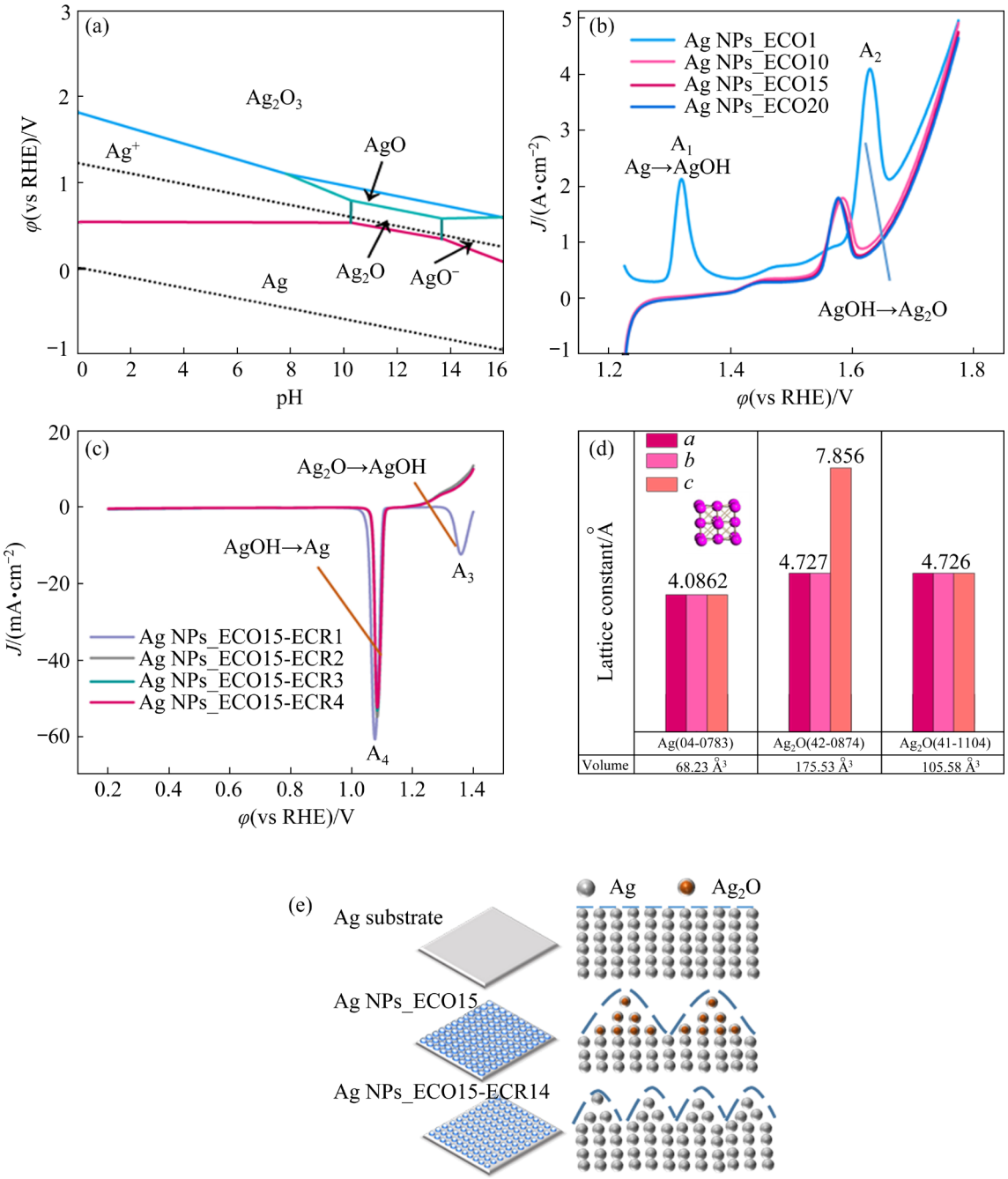

Fig. 2 Potential−pH equilibrium diagram of Ag−H_2O system at 298 K (a), anodic polarization curves of Ag plate in 0.1 mol/L KOH solution at 298 K (scan rate: 20 mV/s) (b), cathodic polarization curves of Ag NPs_ECO15 (c), comparison of lattice parameter and cell volume of metallic Ag and Ag_2O (d), and schematic illustration of change in morphology during in-situ ECO and ECR processes (e)

of 13 is selected as the electrolyte for the electrochemical tuning process. In addition to pH, potential is another factor to consider. In order to reduce the occurrence of oxygen evolution reaction at a theoretical potential of 1.23 V (vs RHE), a high potential, beyond 1.5 V (vs RHE) where the overpotential of oxygen evolution reaction is taken into account, will be unfavorable to the formation of AgO and Ag_2O_3.

This electrochemically driven phase transition process can be further verified by the linear sweep voltammetry (LSV) measurement recorded on the Ag substrate. As shown in Fig. 2(b), with the increase in the potential exceeding 1.25 V (vs RHE), prominent oxidation waves (A_1 and A_2) are observed, which are attributed to the transformation of Ag to AgOH and then to Ag_2O. The two corresponding coupling waves (A_3 and A_4 in Fig. 2(c)) obtained during the reverse scan process are associated with the reversible conversion of Ag_2O to AgOH and following back to Ag [25]. Interestingly, after the LSV measurement, the color of the Ag substrate changed from metallic white to black, suggesting that the surface of the electrode has changed, as confirmed by the corresponding SEM results (Fig. 1).

The next question is what causes such a structure change of Ag during the electrochemically driven phase conversion process. Given the existence of phase transition as indicated by thermodynamic and electrochemical analysis, we quantitatively examine the crystal data of Ag and Ag_2O, as compared in Fig. 2(d). For metallic Ag with a face-centered cubic structure [26,27], the unit cell parameters are determined to be 4.0862 Å × 4.0862 Å × 4.0862 Å with a unit cell volume of 68.23 $Å^3$. In contrast, the cell parameters of the hexagonal Ag_2O are 4.727 Å × 4.727 Å × 7.856 Å, and the cell volume is 175.53 $Å^3$ [28]. As for the cubic Ag_2O [29,30], its cell parameters are 4.726 Å × 4.726 Å × 4.726 Å, and the cell volume is 105.58 $Å^3$. It is clear that the electrochemical oxidation process of the pristine Ag to Ag_2O will lead to the lattice expansion, and the following reversible reduction process will induce severe shrinkage. In this manner, the variation of volume occurring results in such a structural change. Briefly, the change in the morphological structure of Ag along with phase conversion during the electrochemical redox tuning process can be schematically illustrated in Fig. 2(e).

To confirm the above discussed formation mechanism of Ag nanostructures, we have employed TEM and XRD analyses to follow the changes in microstructure and phase of the samples during the electrochemical redox tuning process. As shown in Fig. 3(a), the sample after the in-situ ECO treatment (Ag NPs_ECO15) shows a network architecture, consisting of irregularly distributed NPs. The associated HRTEM image (Fig. 3(a_1)) exhibits a clear lattice fringe with a distance of 0.272 nm, corresponding to lattice plane of Ag_2O (111) [27,31]. With the ECR treatment, a network structure assembled with more uniformly distributed NPs for Ag NPs_ECO15-ECR4 is observed (Fig. 3(b)). Moreover, the ECR treatment leads to in-situ phase conversion from Ag_2O to Ag, as proved by the corresponding HRTEM result (Fig. 3(b_1)). The lattice fringe with a distance of 0.236 nm could be attributed to crystallographic plane of Ag (111) [32]. The fast Fourier transform (FFT) image (inset of Fig. 3(b_1)) displays a hexagonal spot pattern, revealing the single-crystal feature of the NPs. Such a phase conversion process is also identified by using XRD. The XRD patterns of the Ag substrate, Ag NPs_ECO15, and Ag NPs_ECO15-ECR4 are compared in Fig. 4. As expected, newly formed characteristic diffraction peaks of Ag_2O (JCPDS 41-1104 and JCPDS 42-0874) [28,29] are noticed, revealing that in-situ ECO results in the formation of Ag_2O on the surface. After the subsequent ECR treatment, the formed Ag_2O can be converted back into Ag. Both the pristine Ag substrate and the Ag NPs_ECO15-ECR4 have a face-centered cubic crystal structure (JCPDS 04-0873) [26,27]. Notably, the diffraction peaks of Ag NPs_ECO15-ECR4 become wider than those of the Ag substrate (inset of Fig. 4), suggesting that more refined grains are formed in comparison to the Ag substrate, according to the Scherrer formula [33,34], in accordance with the SEM and TEM results. Taken together, it reveals that such an electrochemical redox process induces a reversible in-situ phase conversion, $Ag \rightleftharpoons Ag_2O$, which gives rise to distinct surface reconstruction and thus creates a porous network assembled with highly dispersed NPs.

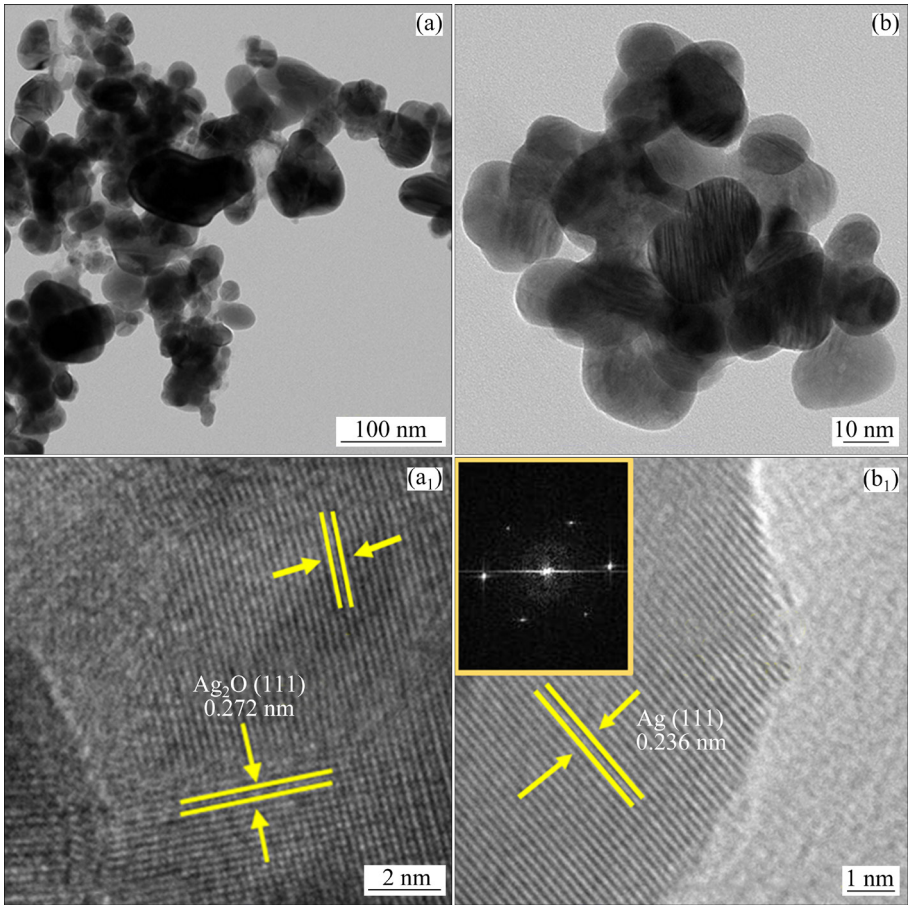

Fig. 3 TEM and HRTEM images of Ag NPs_ECO15 (a, a_1) and Ag NPs _ECO15-ECR4 (b, b_1), respectively (The inset of b_1 shows the associated FFT pattern)

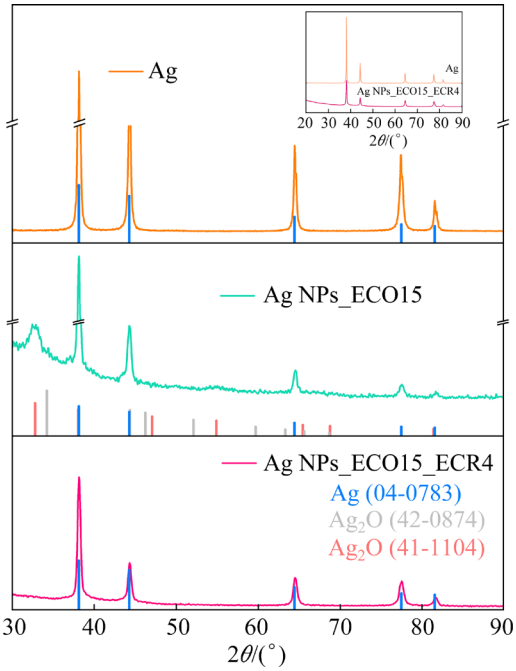

Fig. 4 XRD patterns of pristine Ag substrate, Ag NPs_ECO15, and Ag NPs_ECO15-ECR4, respectively (The inset is a comparison chart of the peak intensity of Ag substrate and Ag NPs_ECO15-ECR4)

3.2 Structural evolution

To further gain insight into the structural evolution during the electrochemical redox (ECO and ECR) process, the morphological and topographical changes at different stages were characterized via SEM and AFM. Upon applying an electrochemical procedure for ECO treatment, significant morphology changes are obviously observed according to Fig. 5. It turns out that the ECO is mainly responsible for the surface reconstruction to form a highly porous architecture, which should be related to the crystal growth of Ag_2O during the oxidation reaction process. The surface structure is obviously coarsened and tends to be homogenized with the advance of the in-situ oxidation process, which indicates the completion of the interfacial phase transformation. The AFM images further recorded the surface topographical changes of the ECO-treated samples obtained at different degrees of oxidation (Fig. 6), achieved by varying the treatment time. The corresponding cross-section analysis in the “height mode” (Inset in

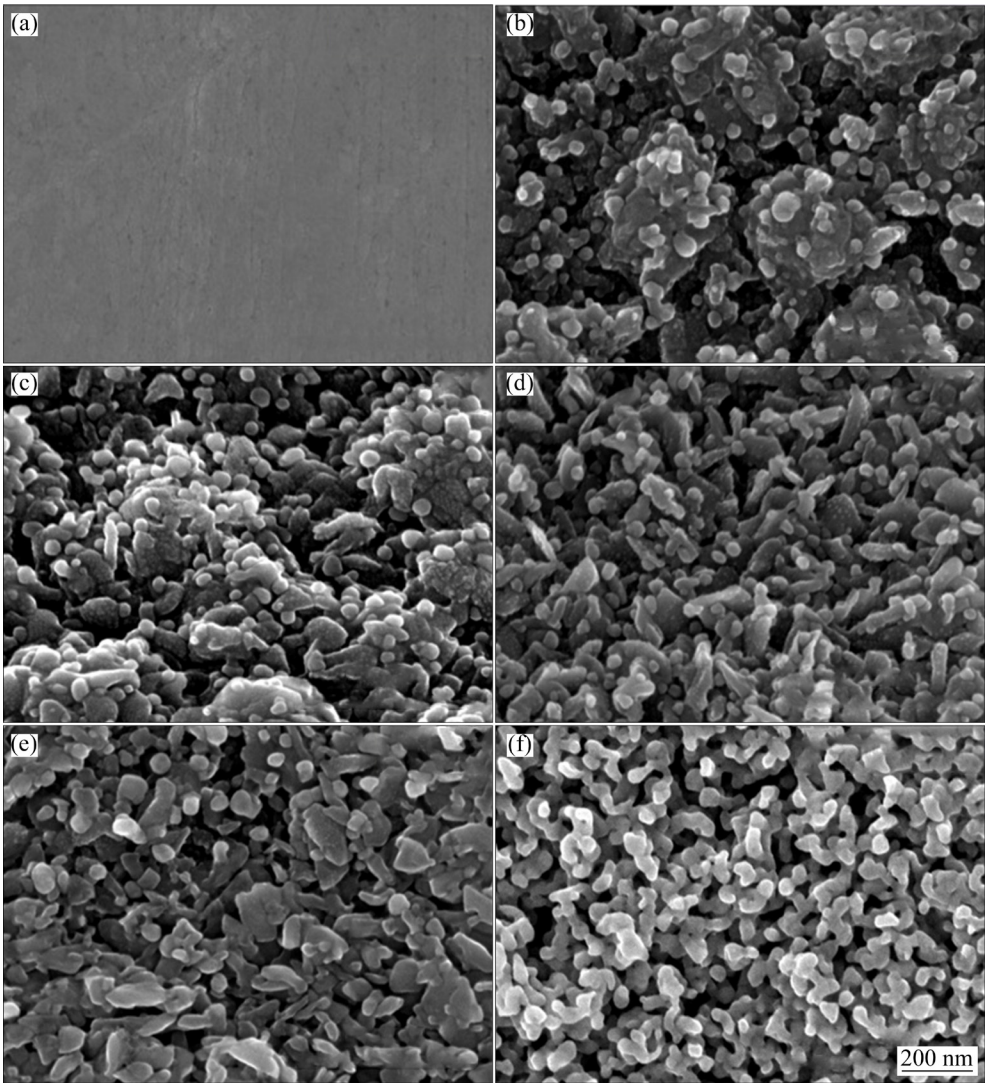

Fig. 5 SEM images of smooth Ag (a), Ag NPs_ECO1 (b), Ag NPs_ECO5 (c), Ag NPs_ECO10 (d), Ag NPs_ECO15 (e), and Ag NPs_ECO15-ECR4 (f)

Fig. 6) reveals the flatness of the height distribution. The fresh Ag substrate has a small surface roughness (R_a) of 3.58 nm, which is found to increase significantly with the proceeding of the in-situ ECO (Fig. 7). The maximum value is reached after 10 times of ECO operation, for which a porous structure with a deeper thickness (peak to valley height) of ~300 nm is obtained. Further increasing the ECO times to 15, these big pores on the surface are filled due to the continuous expansion on the volume of the formed Ag_2O crystals. Consequently, the corresponding R_a reduces.

Following the ECO treatment, the subsequent ECR is also found to affect the final Ag nanostructure. As shown in Figs. 8(a−d), the pristine Ag NPs with large crystal grains for the Ag NPs_ECO15 are gradually broken into smaller ones, and developed into highly dispersed Ag NPs packed porous structure after successive 4 times of ECR. This change is mainly due to the phase transition along with crystal volume shrinkage caused by the ECR process. Further ECR (5 times) leads to the agglomeration of the formed Ag NPs (Fig. 8(e)). According to the XRD results, as displayed in Fig. 4, the electrochemically formed Ag_2O can be completely reduced to Ag, after 4 times of ECR. Such a highly porous architecture for Ag NPs_ECO15-ECR4 after continuous reduction modification suggests a larger surface-active area. Accordingly, its roughness is observed to increase compared to that of Ag NPs_ECO15 (Fig. 7). Moreover, the preliminary ECO treatment provides a framework for the subsequent ECR to refine the structure. As proved by the associated SEM images

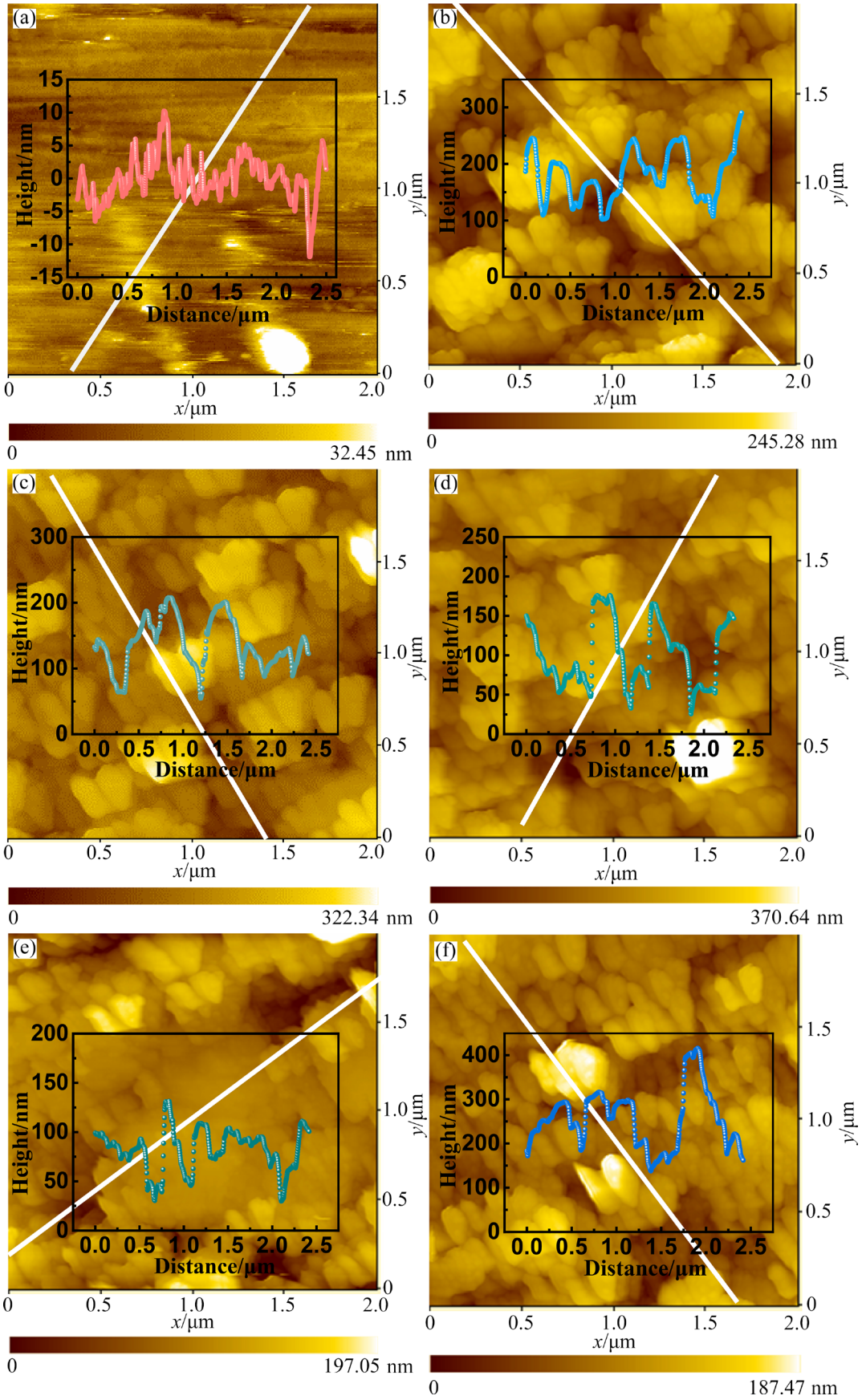

Fig. 6 Top-view AFM images in "height mode" with inset showing corresponding cross-section along line: (a) Smooth Ag; (b) Ag NPs_ECO1; (c) Ag NPs_ECO5; (d) Ag NPs_ECO10; (e) Ag NPs_ECO15; (f) Ag NPs_ECO15-ECR4

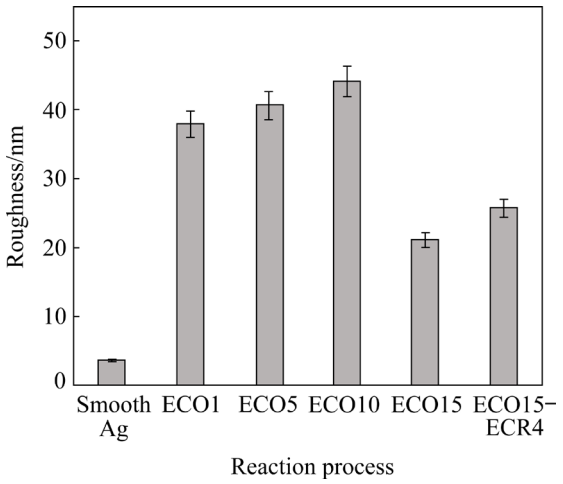

Fig. 7 Roughness change of samples obtained at different stages

(Figs. 8(f−j)), ECR operation on the sample after moderate oxidation treatment (15 ECO processes) is required to form a well-defined highly porous surface. When the oxidation is inadequate (1−10 ECO processes) or excessive (20 or more ECO processes), the NPs generated on the surface are easy to aggregate after ECR, making the structure not fully utilized. These observations indicate that moderate oxidation and reduction of the pristine Ag electrode by controllable electrochemical redox tuning process plays a critical role in constructing a highly dispersed Ag NPs packed porous structure.

To assess the electrochemical surface-active area (ECSA) of the Ag samples with different treatments, a cyclic voltammogram method (Figs. 9(a−c)) is used to measure the double-layer capacitance value (C_{dl}), which is linearly proportional relation to the ECSA, by scanning in the non-Faraday region at different scanning rates (from 20 to 200 mV/s). Based on the fitted capacitances (1/2 slope, Fig. 9(d)), the ECSA of Ag NPs_ECO15 (C_{dl}=0.591 mF/cm^2) is about 6.88-fold larger than that of the pristine Ag substrate (C_{dl}=0.075 mF/cm^2). Subsequent in-situ ECR results in further increased ECSA for Ag NPs_ECO15-ECR4 to 0.725 mF/cm^2, almost 9.6 times that of the Ag substrate. The enhanced ECSA could be related to the surface reconstruction caused by the electrochemical redox tuning process, which leads to the formation of highly porous architecture with abundant exposed sites, as confirmed by the SEM and TEM observations (Fig. 1(c) and Fig. 3(b)). This result reveals that the electrochemical redox tuning process contributes to the clearly enhanced ECSA and active sites of the Ag NPs_ ECO15-ECR4 for the potential application in large-area SERS platform.

3.3 Raman scattering performance

The performance of the electrochemical redox treated Ag electrode as the SERS substrate by using R6G as the probe molecule was evaluated. Smooth Ag substrate was included for comparison. Figure 10 shows the typical SERS spectra of R6G obtained at different concentrations of 1×10^{-9} mol/L for Ag NPs_ECO15-ECR4 and 1×10^{-1} mol/L for smooth Ag, respectively. The characteristic SERS spectra of R6G with the peak positions observed at 1187, 1312, 1365, 1512, 1509, and 1652 cm^{-1} on both electrodes are consistent with the data reported in the literature [5,35]. It is clear that the prepared Ag NPs_ECO15-ECR4 as SERS substrate has a good enhancement effect. The E_f value of Ag NPs_ECO15-ECR4 for R6G molecules is estimated to be 1.32×10^8 by calculating the Raman enhancement factor at the band of 1652 cm^{-1}.

To further evaluate the lowest detectable limit of the Ag NPs_ECO15-ECR4, the concentration of R6G was decreased stepwise (from 1×10^{-6} to 1×10^{-9} mol/L), as shown in Fig. 11(a). As the concentration gradually decreased to 1×10^{-9} mol/L, no obvious Raman scatting signal can be observed, suggesting that the detection concentration of R6G for Ag NPs_ECO15-ECR4 is as low as 1×10^{-9} mol/L. The SERS intensity at 1652 cm^{-1} displays an excellent linear correlation with the R6G concentration ranging from 1×10^{-6} to 1×10^{-9} mol/L (Fig. 11(b)). The fitting linear regression equation is $y=-0.693x+8.109$ (y=lg I_R and x=−lg c_{R6G}), with a squared correlation coefficient of 0.998. The detection limit is derived to be 5.44×10^{-10} mol/L, according to the 3 times signal-to-noise ratio rule [36]. These results show that the synthesized Ag NPs_ECO15-ECR4 exhibits super-SERS sensitivity. Impressively, the detection limit and E_f values for the Ag NPs-based SERS substrate created in this study are comparable to recent reports on Raman signal enhancement materials, as compared in Fig. 12. The ultrahigh Raman sensitivity of the synthesized Ag NPs-based electrode should be related to the well-arranged porous architectures assembled with the tiny NPs,

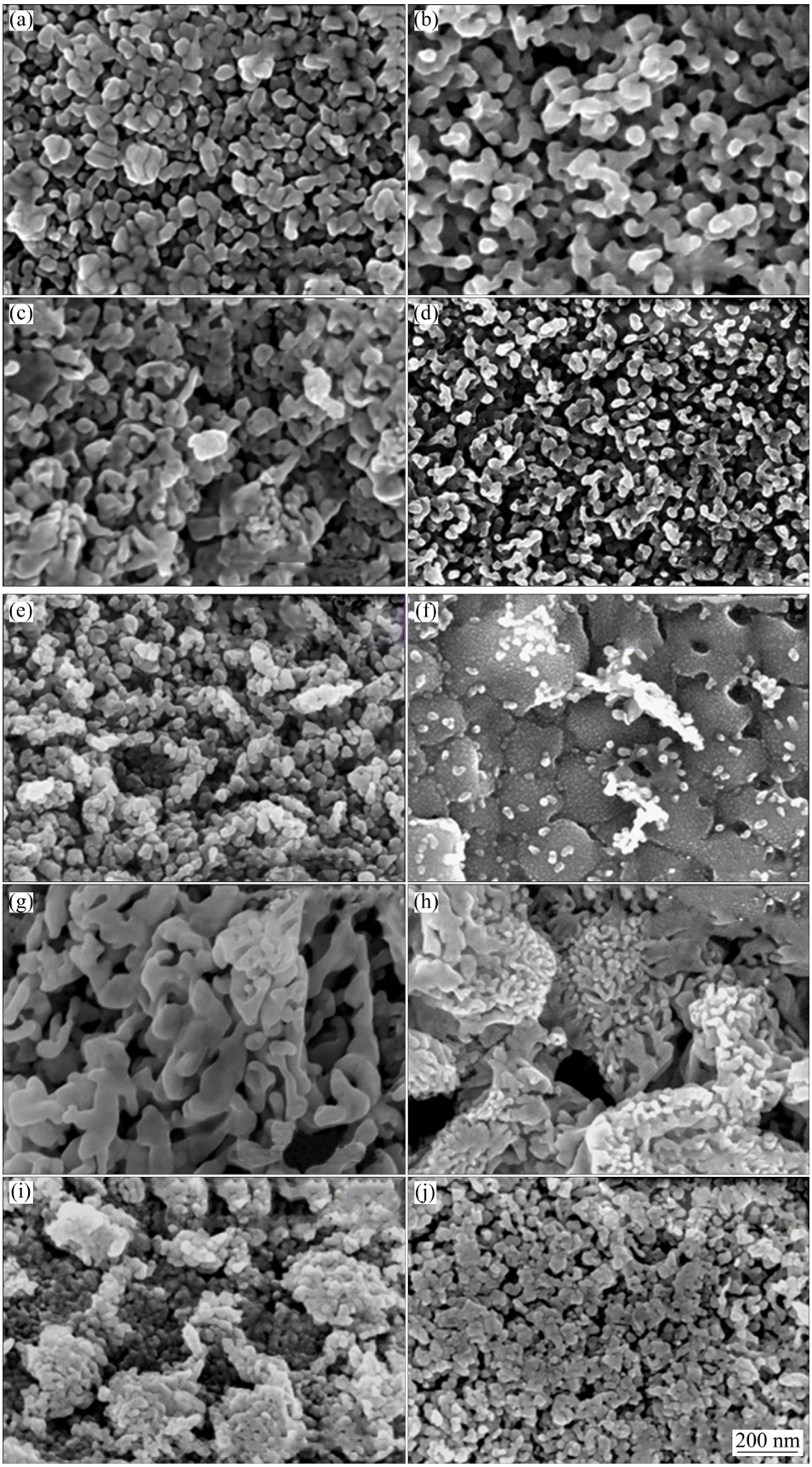

Fig. 8 SEM images of different samples: (a) Ag NPs_ECO15-ECR1; (b) Ag NPs_ECO15-ECR2; (c) Ag NPs_ECO15-ECR3; (d) Ag NPs_ECO15-ECR4; (e) Ag NPs_ECO15-ECR5; (f) Ag NPs_ECO1-ECR4; (g) Ag NPs_ECO3-ECR4; (h) Ag NPs_ECO5-ECR4; (i) Ag NPs_ECO10-ECR4; (j) Ag NPs_ECO20-ECR4

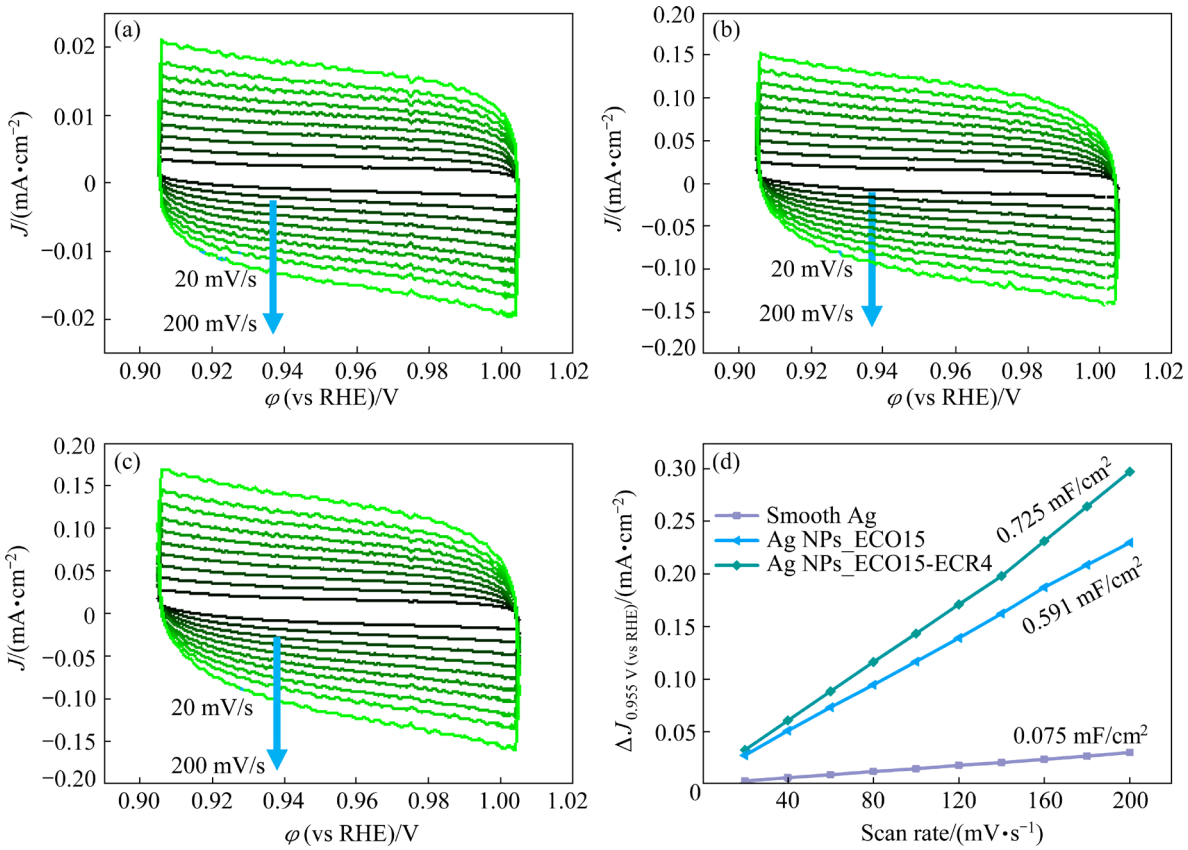

Fig. 9 Cyclic voltammograms of smooth Ag (a), Ag NPs_ECO15 (b), Ag NPs_ECO15-ECR4 (c) in 0.1 mol/L KOH at various scanning rates from 20 mV/s to 200 mV/s, within potential range of 0.905−1.005 V (vs RHE) where no faradaic process is observed, and differences in current density at 0.955 V (vs RHE) ($\Delta J=J_a-J_c$) plotted against scan rate (d)

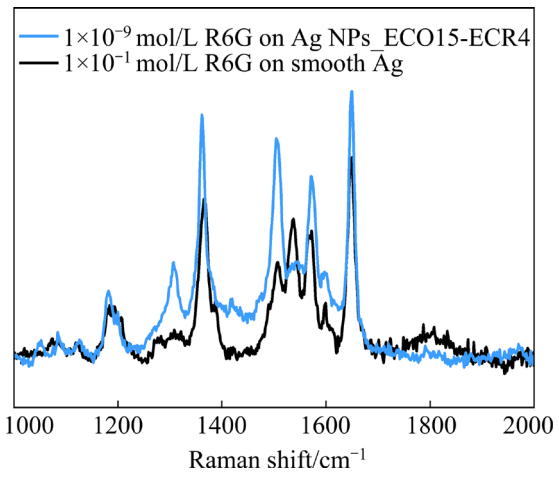

Fig. 10 Raman spectra of 1×10^{-1} mol/L R6G dispersed on smooth Ag substrate and 1×10^{-9} mol/L R6G dispersed on Ag NPs_ECO15-ECR4

which provide a large ECSA and abundant active sites. In addition, the highly porous structure with open pores facilitates mass transport for high-sensitive molecule detection.

4 Conclusions

(1) Ag NPs-packed porous films could be facilely synthesized through a simple, controllable in-situ electrochemical redox tuning approach in 0.1 mol/L KOH solution at room temperature.

(2) The electrochemical redox tuning process induces a reversible in-situ phase conversion, $Ag\rightleftharpoons Ag_2O$ on the surface, which gives rise to distinct surface reconstruction and creates an open porous network assembled with highly dispersed Ag NPs.

(3) The fabricated Ag NPs-packed porous film using the methodology proposed as a SERS electrode can detect the limit concentration of 5.44×10^{-10} mol/L for R6G. In addition, the Ag NPs substrate has a very high enhancement factor of 1.32×10^{8}.

(4) The novel manufacture proposed here may open up a facile scalable technique for the design and fabrication of advanced self-assembly Ag-based electrodes for practical SERS applications.

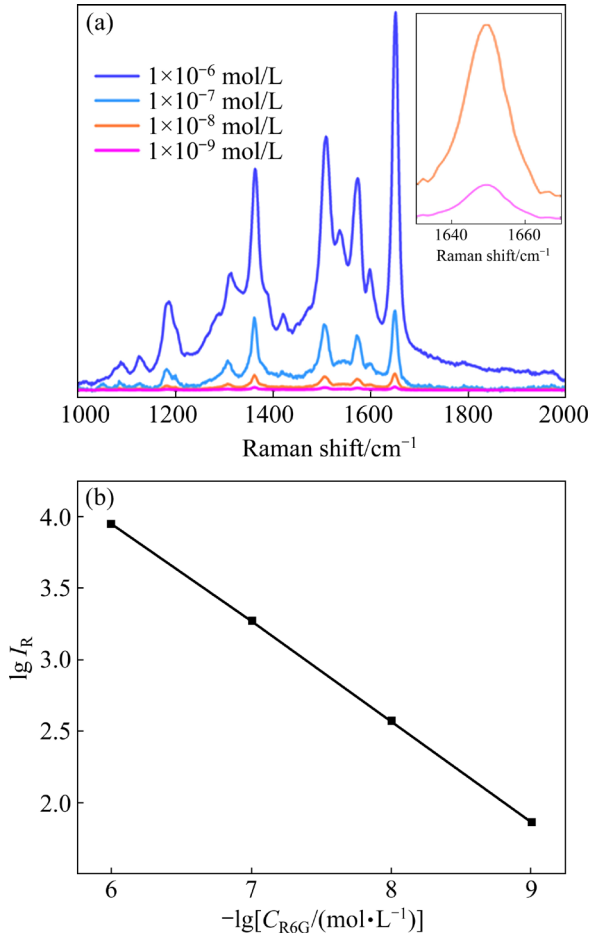

Fig. 11 Raman spectra of different concentrations of R6G molecules dispersed on Ag NPs_ECO15-ECR4 (a) and logarithm of Raman peak intensity at 1652 cm^{-1} versus logarithmic concentration of R6G (b)

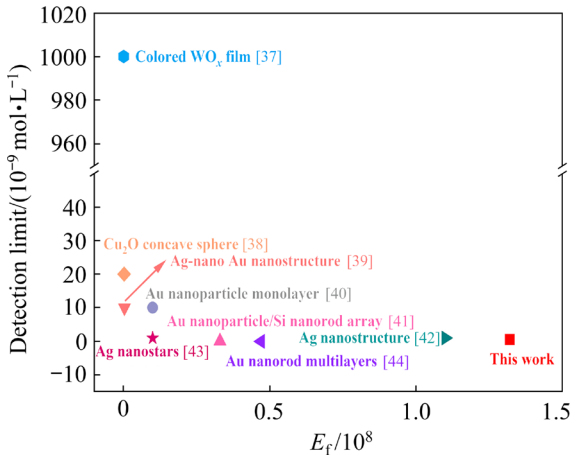

Fig. 12 Comparison of detection limits and E_f values of Ag NPs_ECO15-ECR4 with colored WO_x film [37], Cu_2O concave sphere [38], Ag-nano Au nanostructure [39], Au nanoparticle monolayer [40], Au nanoparticle/Si nanorod array [41], Ag nanostructure [42], Ag nanostars [43] and Au nanorod multilayers [44]

Acknowledgments

The authors gratefully acknowledge the financial support from the National Natural Science Foundation of China (No. 21962008), the Yunnan Province Excellent Youth Fund Project, China (No. 202001AW070005), the Candidate Talents Training Fund of Yunnan Province, China (Nos. 2017PY269SQ, 2018HB007), and the Yunnan Ten Thousand Talents Plan Young & Elite Talents Project, China (No. YNWR-QNBJ-2018- 346).

References

[1] SEH Z W, KIBSGAARD J, DICKENS C F, CHORKENDORFF I, NØRSKOV J K, JARAMILLO T F. Combining theory and experiment in electrocatalysis: Insights into materials design [J]. Science, 2017, 355(6321): eaad4998.

[2] ZHOU H H, LI Y L, HUANG J Q, FANG C X, SHAN D, KUANG Y F. Ag−Ni alloy nanoparticles for electrocatalytic reduction of benzyl chloride [J]. Transactions of Nonferrous Metals Society of China, 2015, 25(12): 4001−4007.

[3] SAGITHA P, SARADA K, MURALEEDHARAN K. One-pot synthesis of poly vinyl alcohol (PVA) supported silver nanoparticles and its efficiency in catalytic reduction of methylene blue [J]. Transactions of Nonferrous Metals Society of China, 2016, 26(10): 2693−2700.

[4] MA C X, TRUJILLO M J, CAMDEN J P. Nanoporous silver film fabricated by oxygen plasma: A facile approach for SERS substrates [J]. ACS Applied Materials & Interfaces, 2016, 8(36): 23978−23984.

[5] LIU Y, TIAN X R, GUO W R, WANG W Q, GUAN Z Q, XU H X. Real-time Raman detection by the cavity mode enhanced Raman scattering [J]. Nano Research, 2019, 12: 1643−1649.

[6] TIAN Q H, DENG D, LI Y, GUO X Y. Preparation of ultrafine silver powders with controllable size and morphology [J]. Transactions of Nonferrous Metals Society of China, 2018, 28(3): 524−533.

[7] QIU H J, LI X, XU H T, ZHANG H J, WANG Y. Nanoporous metal as a platform for electrochemical and optical sensing [J]. Journal of Materials Chemistry A, 2014, 2(46): 9788−9799.

[8] DING Y, CHEN M W. Nanoporous metals for catalytic and optical applications [J]. MRS Bulletin, 2009, 34(8): 569−576.

[9] NOVARA C, DALLA MARTA S, VIRGA A, LAMBERTI A, ANGELINI A, CHIADÒ A, RIVOLO P, GEOBALDO F, SERGO V, BONIFACIO A, GIORGIS F. SERS-active Ag nanoparticles on porous silicon and PDMS substrates: A comparative study of uniformity and Raman efficiency [J]. The Journal of Physical Chemistry C, 2016, 120(30): 16946−16953.

[10] WANG J Q, LI Z, DONG C K, FENG Y, YANG J, LIU H, DU X W. Silver/copper interface for relay electroreduction of carbon dioxide to ethylene [J]. ACS Applied Materials &

Interfaces, 2019, 11(3): 2763−2767.

[11] HUANG J F, WU Y C. Tunable Ag micromorphologies show high activities for electrochemical H_2 evolution and CO_2 electrochemical reduction [J]. ACS Sustainable Chemistry & Engineering, 2019, 7(6): 6352−6359.

[12] LIU C, YIN H B, WANG A L, WU Z N, WU G, JIANG T, SHEN Y T, JIANG T S. Size-controlled preparation of hollow silica spheres and glyphosate release [J]. Transactions of Nonferrous Metals Society of China, 2012, 22(5): 1161−1168.

[13] ZHENG M, WANG Z S, ZHU Y W. Preparation of silver nanoparticle via active template under ultrasonic [J]. Transactions of Nonferrous Metals Society of China, 2006, 16(6): 1348−1352.

[14] SHIN K, LEACH K A, GOLDBACH J T, KIM D H, JHO J Y, TUOMINEN M, HAWKER C J, RUSSELL T P. A simple route to metal nanodots and nanoporous metal films [J]. Nano Letters, 2002, 2(9): 933−936.

[15] ERLEBACHER J, AZIZ M J, KARMA A, DIMITROV N, SIERADZKI K. Evolution of nanoporosity in dealloying [J]. Nature, 2001, 410(6827): 450−453.

[16] DING Y, ERLEBACHER J. Nanoporous metals with controlled multimodal pore size distribution [J]. Journal of the American Chemical Society, 2003, 125(26): 7772−7773.

[17] XUE Y P, SCAGLIONE F, PASCHALIDOU E M, RIZZI P, BATTEZZATI L. Excellent surface enhanced Raman scattering obtained with nanoporous gold fabricated by chemical de-alloying [J]. Chemical Physics Letters, 2016, 665: 6−9.

[18] CHEN F, CHEN X, ZOU L J, YAO Y, LIN Y J, SHEN Q, LAVERNIA E J, ZHANG L M. Fabrication and mechanical behavior of bulk nanoporous Cu via chemical de-alloying of Cu−Al alloys [J]. Materials Science and Engineering A, 2016, 660: 241−250.

[19] ZHANG Q B, ABBOTT A P, YANG C. Electrochemical fabrication of nanoporous copper films in choline chloride-urea deep eutectic solvent [J]. Physical Chemistry Chemical Physics, 2015, 17(22): 14702−14709.

[20] PUGH D V, DURSUN A, CORCORAN S G. Formation of nanoporous platinum by selective dissolution of Cu from $Cu_{0.75}Pt_{0.25}$ [J]. Journal of Materials Research, 2003, 18(1): 216−221.

[21] GU Y, DONG C S, ZHONG M L, MA M X, LI L, LIU W. Fabrication of nanoporous manganese by laser cladding and selective electrochemical de-alloying [J]. Applied Surface Science, 2011, 257(8): 3211−3215.

[22] HUANG J F, WU Y C. Making Ag present Pt-like activity for hydrogen evolution reaction [J]. ACS Sustainable Chemistry & Engineering, 2018, 6(7): 8285−8290.

[23] LE RU E C, BLACKIE E, MEYER M, ETCHEGOIN P G. Surface enhanced Raman scattering enhancement factors: A comprehensive study [J]. The Journal of Physical Chemistry C, 2007, 111(37): 13794−13803.

[24] LI X L, ZHANG Y Z, SHEN Z X, FAN H J. Highly ordered arrays of particle-in-bowl plasmonic nanostructures for surface-enhanced Raman scattering [J]. Small, 2012, 8(16): 2548−2554.

[25] GUO J S, HSU A, CHU D, CHEN R R. Improving oxygen reduction reaction activities on carbon-supported Ag nanoparticles in alkaline solutions [J]. The Journal of Physical Chemistry C, 2010, 114(10): 4324−4330.

[26] WANG Q, CHEN F Y, LIU Y X, ZHANG N, AN L, JOHNSTON R L. Bifunctional electrocatalysts for oxygen reduction and borohydride oxidation reactions using Ag_3Sn nanointermetallic for the ensemble effect [J]. ACS Applied Materials & Interfaces, 2017, 9(41): 35701−35711.

[27] THANH T D, CHUONG N D, HIEN H V, KIM N H, LEE J H. CuAg@Ag core-shell nanostructure encapsulated by N-doped graphene as a high-performance catalyst for oxygen reduction reaction [J]. ACS Applied Materials & Interfaces, 2018, 10(5): 4672−4681.

[28] AL-KUHAILI M F. Characterization of thin films produced by the thermal evaporation of silver oxide [J]. Journal of Physics D: Applied Physics, 2007, 40(9): 2847−2853.

[29] IDA Y, WATASE S, SHINAGAWA T, WATANABE M, CHIGANE M, INABA M, TASAKA A, IZAKI M. Direct electrodeposition of 1.46 eV bandgap silver(I) oxide semi-conductor films by electrogenerated acid [J]. Chemistry of Materials, 2008, 20(4): 1254−1256.

[30] LI S J, HU S W, XU K, JIANG W, LIU Y, LENG Z, LIU J S. Construction of fiber-shaped silver oxide/tantalum nitride p-n heterojunctions as highly efficient visible-light-driven photocatalysts [J]. Journal of Colloid and Interface Science, 2017, 504: 561−569.

[31] WU X Q, CHEN F Y, ZHANG N, QASEEM A, JOHNSTON R L. A silver–copper metallic glass electrocatalyst with high activity and stability comparable to Pt/C for zinc–air batteries [J]. Journal of Materials Chemistry A, 2016, 4(9): 3527−3537.

[32] LEI H, SINGH SIWAL S S, ZHANG X Y, ZHANG Q B. Compositional and morphological engineering of in-situ-grown Ag nanoparticles on Cu substrate for enhancing oxygen reduction reaction activity: A novel electrochemical redox tuning approach [J]. Journal of Colloid and Interface Science, 2020, 571: 1−12.

[33] KWON N H, YIN H, VAVROVA T, LIM J H W, STEINER U, GROBÉTY B, FROMM K M. Nanoparticle shapes of $LiMnPO_4$, Li^+ diffusion orientation and diffusion coefficients for high volumetric energy Li^+ ion cathodes [J]. Journal of Power Sources, 2017, 342: 231−240.

[34] THUY N T, CONG B T, LE MINH D. The structural and magnetic properties of the double rare earth elements $La_{1-x}Nd_xFeO_3$ nanoparticles [J]. ISRN Materials Science, 2012, 2012: 1−6.

[35] HILDEBRANDT P, STOCKBURGER M. Surface-enhanced resonance Raman spectroscopy of Rhodamine 6G adsorbed on colloidal silver [J]. The Journal of Physical Chemistry, 1984, 88(24): 5935−5944.

[36] PEARMAN W F, ANGEL S M, FERRY J L, HALL S. Characterization of the Ag mediated surface-enhanced Raman spectroscopy of saxitoxin [J]. Applied Spectroscopy, 2008, 62(7): 727−732.

[37] CONG S, WANG Z, GONG W B, CHEN Z G, LU W B, LOMBARDI J R, ZHAO Z G. Electrochromic semiconductors as colorimetric SERS substrates with high reproducibility and renewability [J]. Nature Communications, 2019, 10(1): 678.

[38] LI X X, SHANG Y, LIN J, LI A R, WANG X T, LI B, GUO L. Temperature-induced stacking to create Cu_2O concave sphere for light trapping capable of ultrasensitive single-particle surface-enhanced Raman scattering [J]. Advanced Functional Materials, 2018, 28(33): 1801868.
[39] ZHAO H Z, XU Y, WANG C Y, WANG R, XIANG S T, CHEN L. Design and fabrication of a microfluidic SERS chip with integrated Ag film@nanoAu [J]. RSC Advances, 2016, 6(17): 14105−14111.
[40] YANG G, NANDA J, WANG B Y, CHEN G, HALLINAN D T, JR. Self-assembly of large gold nanoparticles for surface-enhanced Raman spectroscopy [J]. ACS Applied Materials & Interfaces, 2017, 9(15): 13457−13470.
[41] LIN D D, WU Z L, LI S J, ZHAO W Q, MA C J, WANG J, JIANG Z M, ZHONG Z M, ZHENG Y B, YANG X J. Large-area Au-nanoparticle-functionalized Si nanorod arrays for spatially uniform surface-enhanced Raman spectroscopy [J]. ACS Nano, 2017, 11(2): 1478−1487.
[42] BAI S, SERIEN D, MA Y, OBATA K, SUGIOKA K. Attomolar sensing based on liquid interface-assisted surface-enhanced Raman scattering in microfluidic chip by femtosecond laser processing [J]. ACS Applied Materials & Interfaces, 2020, 12(37): 42328−42338.
[43] OLIVEIRA M J, QUARESMA P, de ALMEIDA M P, ARAÚJO A, PEREIRA E, FORTUNATO E, MARTINS R, FRANCO R, ÁGUAS H. Office paper decorated with silver nanostars—An alternative cost effective platform for trace analyte detection by SERS [J]. Scientific Reports, 2017, 7(1): 2480.
[44] JEONG J W, ARNOB M M, BAEK K M, LEE S Y, SHIH W C, JUNG Y S. 3D cross-point plasmonic nanoarchitectures containing dense and regular hot spots for surface-enhanced Raman spectroscopy analysis [J]. Advanced Materials, 2016, 28(39): 8695−8704.

原位电化学氧化还原制备高性能表面增强拉曼散射银纳米颗粒薄膜

雷 浩[1,2]，李 艳[1]，郭孟伟[1]，张启波[1,3]

1. 昆明理工大学 冶金与能源工程学院 离子液体冶金实验室，昆明 650093；
2. 哈尔滨工业大学(深圳) 深圳市柔性印刷电子技术研究中心，深圳 518055；
3. 昆明理工大学 云南省复杂有色金属资源清洁利用国家重点实验室，昆明 650093

摘 要：在适当 pH 范围的碱性溶液中，通过施加氧化还原电位实现光滑 Ag 基体原位转化为纳米多孔结构，此纳米多孔结构由平均尺寸为 21.88 nm 的 Ag 纳米颗粒(Ag NPs)组成。系统研究电化学氧化还原调控制备 Ag NPs 电极过程中 Ag 基体的物相和形貌演化过程：在可控氧化还原电位的作用下，光滑 Ag 基体首先被电化学氧化为 Ag_2O，引起晶胞体积膨胀，随后电化学还原生成金属 Ag，伴随体积收缩。晶胞体积在可逆电化学转化过程中的膨胀和收缩导致 Ag 基体表面原位形成高孔隙结构。采用该方法制备的 Ag NPs 电极呈现优异的表面增强拉曼散射性能，将其作为衬底检测罗丹明 6G 溶液时，拉曼光谱检测限可低至 5.44×10^{-10} mol/L。

关键词：电化学氧化还原；银纳米颗粒；多孔薄膜；表面增强拉曼散射性能

(Edited by Wei-ping CHEN)